Lanthanide–Cyclen–Camptothecin Nanocomposites for Cancer Theranostics Guided by Near-Infrared and Magnetic Resonance Imaging

Yonghong Zhang,‡[1,2] Xia Ma,‡[1] Ho-Fai Chau,‡[1] Waygen Thor,[1] Lijun Jiang,[3] Shuai Zha,[1] Wan-Yiu Fok,[1] Ho-Nam Mak,[1] Junhui Zhang,[3] Jing Cai,[4] Chi-Fai Ng,[5] Hongguang Li,[6] David Parker,*[7] Li Li,*[4] Ga-Lai Law,*[3] and Ka-Leung Wong*[1]

[1]Department of Chemistry, Hong Kong Baptist University, Kowloon Tong, Kowloon, Hong Kong SAR, China.
[2]Key Laboratory of Energy Materials Chemistry, Ministry of Education; Key Laboratory of Advanced Functional Materials, Autonomous Region; Urumqi Key Laboratory of Green Catalysis and Synthesis Technology, College of Chemistry, Xinjiang University, Urumqi, 830046, Xinjiang, China.
[3]Department of Applied Biology and Chemical Technology, The Hong Kong Polytechnic University, Hung Hom, Kowloon, Hong Kong SAR, China.
[4]State Key Laboratory of Oncology in South China, Imaging Diagnosis and Interventional Center, Sun Yat-sen University Cancer Center, Guangzhou 510060, China.
[5]Department of Surgery, The Chinese University of Hong Kong, Shatin, Hong Kong SAR, China.
[6]School of Biotechnology and Health Sciences, Wuyi University, Jiangmen 529020, China.
[7]Department of Chemistry, Durham University, South Road, Durham DH1 3LE, United Kingdom.

ABSTRACT: We have devised a molecular-to-micellar strategy to incorporate a lanthanide nanoplatform for the delivery of an anti-cancer drug that simultaneously offers hybrid near-infrared (NIR) and magnetic resonance imaging (MRI) capabilities with defined lanthanide(III) ratio control. This cancer-selective lanthanide-based self-assembled nanocomposite (**LnNPs**) has been synthesized by conjugating lanthanide-cyclen complexes (**cycLn**) with a well-known drug – camptothecin (**CPT**) – through a redox-sensitive disulfide bond (**-ss-**). By accurately controlling the ratio of Gd(III)- and Yb(III)-complexes, we prepared hybrid nanoparticles (**Gd/YbNPs**) with both NIR and MR imaging properties. The enhanced stability at ultra-low critical aggregation concentrations (CAC), simultaneous optical and MR imaging, improved delivery/chemotherapeutic efficiency, and cancer cell selectivity of such nanomicellar theranostic prodrugs *in vitro* and *in vivo* has thus been achieved and validated. The work provides a blueprint combining stimuli-activated NIR luminescence and real-time MR imaging into a safe and biocompatible nanoplatform for selective cancer treatment. **Keywords:** Nanocomposite, Prodrug, Lanthanide, Theranostics, Multimodal Imaging

Introduction

Recently, lanthanide(III) complexes appear in the limelight for both magnetic resonance (MR) and optical imaging.[1–4] Gadolinium (Gd) based chelates are widely used as contrast agents (CA) to enhance MR image contrast and improve diagnostic accuracy. On the other hand, ytterbium (Yb) based complexes exhibit lanthanide luminescence in the near-infrared (NIR) region, with minimal autofluorescence for optical imaging.[5,6] These two imaging modalities complement each other in terms of resolution and sensitivity. Furthermore, self-assembling and self-delivering activatable macromolecules have attracted much attention over the past decade for drug delivery applications, owing to their ability to encapsulate small molecules in a high-loading and carrier-free manner. This means of delivery is especially useful when the cargo of interest has poor water-solubility, which is the case for most potent anti-cancer drugs. As a result, we set out to devise a dual-functional self-assembled platform for real-time imaging and drug delivery.

While it is common in the literature, especially over the past decade, that lanthanide-doped nanomaterials have been designed and synthesized for dual- or multifunctional platforms, we strongly believe that quantitative control of these nanomaterials greatly hinders their qualitative efficacy. The advantage of doped nanomaterials can in fact be its greatest disadvantage as well: by mixing different Ln^{3+} precursors, different properties can be imparted to the nanomaterials. However, precise control of the ratio of the Ln^{3+} content remains challenging with respect to reproducibility at the synthetic stage, and it is not always possible to guarantee that the ratio of Ln^{3+} precursors is preserved in the isolated product, creating another quality control problem. Without having a well-defined Ln^{3+} ratio, it is impossible to optimize different properties in the same system. Moreover, any toxicity brought about by the leaching of trace amounts of free Ln^{3+} cannot be traced back.

Therefore, in this work, we propose a "proof-of-concept solution" for the development of lanthanide-based dual-functional drug delivery platforms, in the form of self-assembled molecular nanocomposites with defined control of the metal ion ratio.

There have been reports on designing self-assemblies of lanthanide complexes in literature.[7,8] For simple imaging entities, Rao *et al.*, Ye *et al.*, and Meade *et al.*, respectively, have reported smart *in vitro* enzymatic reaction-based self-assembling MRI contrast agent,[9] an *in vivo* self-aggregating fluorogenic small-molecule MR/NIR imaging probe,[10] and a self-assembling AIEgen-Gd/DOTA-peptide-based bimodal luminescence-MRI contrast agent respectively.[11] There have also been literature reports on using Gd-complexes to develop theranostic prodrugs: Shen *et al.* documented a novel MRI theranostic *in vivo* prodrug self-assembled from small amphiphilic Gd/DTPA-CPT conjugates (i.e. acyclic ligand), but their cancer cell selectivity is unknown.[12] Gao *et al.* disclosed an *in vivo* tumor-targeting MRI theranostic biotin-Gd/DOTA-CPT (i.e. cyclic ligand) molecular probe with outstanding results, but the probe cannot self-assemble for better delivery.[13]

Camptothecin CPT, a well-known anti-cancer drug with poor water-solubility, is a naturally occurring compound that possesses high cytotoxicity in many cell lines by targeting DNA topoisomerase I and inducing apoptosis. At equilibrium, CPT exists in the active closed lactone form and an inactive open-carboxylate form. However, the major limitations of the active form, in addition to poor aqueous solubility, includes ready hydrolysis (instability) and poor selectivity towards cancer cells, each of which restrict its full clinical translation.[14–17] Various classes of stimuli-responsive, nanoparticle-based CPT nano-prodrug have been developed as delivery vehicles by self-assembly.[18–20] The CPT encapsulation into amphiphilic micellar/polymeric systems,[21–27] and the formation of amphiphilic polymer-CPT conjugates[28,29,38–40,30–37] represent two promising paradigms. Although each paradigm shows improved chemotherapeutic efficacy of CPT, the former cage systems suffers from either inevitable leakage or loading inefficiency issues, while the latter branched polymeric systems give rise to problems of structural heterogeneity in synthesis combined with the intrinsic unavailability of precise, real-time monitoring of drug release.[41–43]

To integrate these theranostic CPT prodrug advantages whilst addressing the universal shortcoming of an ill-defined metal content ratio in doped/surface-functionalized nanoparticle systems, we have set out to develop one-component, multifunctional, self-assembling theranostic nano-agents, which combine both NIR/MR imaging capacities for real-time monitoring and selective cancer imaging diagnosis and CPT chemotherapy, thereby offering an excellent "all-round" solution.[39,44–51]

In this proof-of-concept study, we decided to use lanthanide–CPT nano-conjugates to demonstrate our model design. We have rationally designed a molecular-to-micellar nanocomposite system, based on the self-assembly of cyclen-based Gd- and Yb-complexes (cycLn) for MR response and NIR imaging properties, respectively, where the metal content ratio can be controlled by mixing at the molecular phase and is determined with its almost uniform micellar size. Cyclen-derived macrocycles are known to be highly stable chelators for Ln^{3+} and their pharmacokinetic properties are well studied; we can control the localization of our nanocomposite without letting it accumulate non-selectively. We conjugated the hydrophobic CPT moiety to the hydrophilic cycLn entity through a disulfide bond linker. Encapsualtion of CPT was automatically achieved when the amphiphilic complexes (**cycLn-ss-CPT**) self-assembled into micellar nanoparticles (**LnNPs**) to reduce injury to normal cells, with the charged cycLn protruding outwards to improve overall water solubility. Under the unique tumor microenvironment, the high local glutathione (GSH) concentration can act as an intracellular trigger for the cleavage of the redox-responsive disulfide bond through a thiol-disulfide exchange reaction.[13,30,54–59,31,35,36,38–40,52,53] Thus, after cellular internalization of **cycLn-ss-CPT** nanoparticles, free CPT can be released *in situ* to kill cancer cells. Meanwhile, T_1-weighted MR images and enhanced NIR imaging intensity and CPT luminescence intensity can be observed within the system.

Hereby, we introduce a direct real-time MRI/Vis/NIR monitoring of cancer-selective controlled releasing systems of the cytotoxic CPT through a self-assembling multimodal theranostic micellar lanthanide–CPT prodrug design, with the lanthanide metal ratio in the nanocomposites **LnNPs** being controllable by this molecular approach. In particular, we have been able to confirm the delivery of **cycLn-ss-CPT** *in vivo* which is highly stable even at ultralow critical aggregation concentrations (CAC).[60,61] This work heralds the vision we have for designing the next generation of drug delivery and theranostic nanoplatforms, with hybrid dual-imaging capabilities, specific anti-cancer effects, and well-defined molecular tunability with control of the metal content ratio.

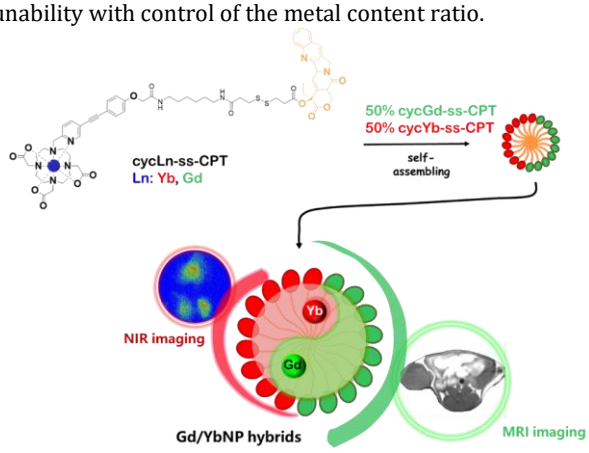

Figure 1. Schematic view of the chemical structure and hybrid MRI/NIR imaging of **Gd/YbNPs**.

Results and discussion

Synthesis of the amphiphiles cycLn-ss-CPT. The amphiphiles **cycLn-ss-CPT** (Ln = Gd for MR imaging, Yb for NIR imaging, and Eu for luminescence analysis) were synthesized *via* a ten-step process (Fig. 1, Schemes S1 and S2). The detailed synthetic procedures are described in the SI. **cycLn-ss-CPT** were purified by preparative high-performance liquid chromatography (HPLC), and characterized by analytical HPLC, HRMS, and FT-IR. UV-Vis also confirmed that **cycLn-ss-CPT** had the characteristic absorption peaks of both cycLn (~ 330 nm) and CPT (~ 360 nm and ~ 380 nm) (Fig. S13, S15 and S18). Emission spectral analysis further verified the successful synthesis, specifically, emission peaks of both cycLn (characteristic emission peaks of Yb and Eu) and CPT (~ 430 nm) were apparent. It was found that the luminescence of CPT was quenched in **cycLn-ss-CPT** compared to free CPT, likely due to the metal quenching effect, although the extent of quenching varied somewhat in the different Ln(III) complexes (Fig. S14, S16, S17, S19, and S20). Hydration numbers of the amphiphiles were calculated by measuring the lifetimes of **cycEu-ss-CPT** in H_2O and D_2O (Fig. S21 and S22; Table S2). The results showed that one H_2O molecule was directly coordinated to the Ln(III) core, consistent

with the requirement of **cycGd-ss-CPT** as an MRI contrast agent.

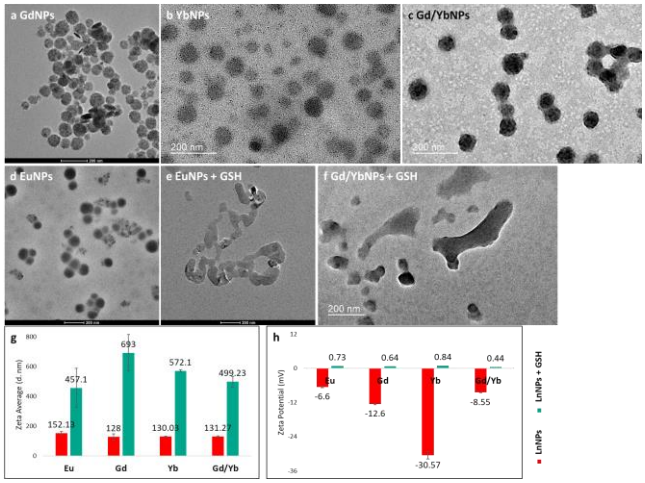

Figure 2. TEM images of (a) **GdNPs**, (b) **YbNPs**, (c) **Gd/YbNPs**, (d) **EuNPs**, (e) **EuNPs** + GSH, and (f) **Gd/YbNPs** + GSH. (g) Size distribution, and (f) Zeta-potential of **EuNPs**, **GdNPs**, **YbNPs**, and **Gd/YbNPs** with GSH (in green bars) and without GSH (in red bars) determined by DLS.

Self-assembly of the amphiphiles cycLn-ss-CPT and its hybrids.

The conjugate **cycLn-ss-CPT** can spontaneously self-assemble to form nanoparticles in aqueous solution in keeping with its amphiphilic nature. **CycLn-ss-CPT** nanoparticles (**LnNPs**) were prepared using the simple and effective dialysis technique (Fig. S7). Briefly, **cycLn-ss-CPT** was dissolved in DMSO and the resulting solution was added dropwise to deionised water in a dialysis tube. The corresponding **Gd/YbNPs** (hybrid) was obtained by removing DMSO through dialysis against water. The CAC value is an important parameter that reflects the self-assembling ability of **cycLn-ss-CPT** and the relative stability of the assembled nanoparticles. The CAC of **cycLn-ss-CPT** was measured to be ~ 0.62 μM using conventional luminescence methods (a pyrene probe). An ultralow CAC was also obtained using gold NPs as the probe,[60] consistent with the remarkable stability of **Gd/YbNPs** and its capability as a delivery platform for CPT (Fig. S4–S6).

Dynamic light scattering (DLS) measurements showed well-defined nanoparticles and revealed that the **Gd/YbNPs** had a hydrophobic diameter of 128 – 152 nm with a zeta potential of -30 mV to -7 mV (**EuNPs**: 152 nm, -7 mV; **GdNPs**: 128 nm, -13 mV; **YbNPs**: 130 nm, -31 mV; **Gd/YbNPs**: 131 nm, -9 mV) (Figs. 2g and h). Transmission electron microscopy (TEM) studies suggested that **Gd/YbNPs** were spherical, with relatively uniform sizes of *ca.* 59 – 87 nm, i.e. 87 nm for **EuNPs**, 72 nm for **GdNPs**, 59 nm for **YbNPs**, 75 nm for **Gd/YbNPs**. It was found that without the hydrophobic part (CPT), cycLn alone could not form nanoparticles (Fig. S8). Notably, the size of **Gd/YbNPs** measured by DLS was around twice the size observed in TEM. The differences between DLS- and TEM-determined sizes relate to the fact that micellar aggregations greatly shrink when dried in the vacuum state required for TEM measurements.

Drug release and stability of Gd/YbNPs.

We next evaluated the CPT release by **Gd/YbNPs** *via* DLS, TEM and luminescence analyses. As shown in Fig. 2g, a significant size increase was observed for every **LnNP** in the presence of GSH, including the **Gd/YbNPs**, where the diameter increased from 131 nm to 499 nm. The zeta potential of **Gd/YbNPs** also increased with GSH (Fig. 2h). Furthermore, TEM images showed the collapse of the nanoparticle structures upon GSH treatment, resulting in the rearrangement of the hydrophobic fragments to a large aggregating form (Figs. 2e and f).

The cleavage of the disulfide bond and release of CPT was further investigated by luminescence analysis. As clearly shown in Fig. 3a, GSH treatment of LnNPs caused an obvious increase in the CPT luminescence intensity at 430 nm, when the CPT moiety was directly excited (λ_{ex}: 370 nm). Impressively, the addition of GSH also caused a luminescence intensity increase of the Eu(III) and Yb(III) emission, when the ligand was excited (λ_{ex}: 330 nm) (Fig. 3b and S10), given that the molar extinction coefficient (ε) and the luminescence quantum yield (ϕ) of **YbNPs** in water was found to be 14864 $M^{-1}cm^{-1}$ and 0.0087, respectively. Such behaviour is likely due to intramolecular energy transfer from the ligand in **cycLn-ss-CPT** to both the CPT moiety and the Ln(III) ion. As reflected in Fig. S19 when the ligand is excited at 330 nm, both CPT and Eu(III) emission are presented in the spectra of **cycEu-ss-CPT**; when CPT was released, upon excitation at 330 nm, excited energy from the ligand is no longer transferred to CPT but instead is entirely transferred to the Ln(III) ion, demonstrating the responsiveness of lanthanide emission to the GSH treatment.

It is well-known that the active lactone form of CPT hydrolyzes quickly in phosphate-buffered saline (PBS) with a reported half-life of ~ 25 min, and only 17% of the lactone form exists at equilibrium. Accordingly, we examined the stability of **Gd/YbNPs** in solution (PBS) and *ex vivo* (mice blood serum). By monitoring the luminescence intensity at 430 nm, no obvious intensity increase from **GdNPs** in either PBS or mice blood serum over 4 days was observed (Fig. 3c). Also, DLS analysis showed that the **GdNPs** maintained their hydrodynamic size under these conditions, consistent with colloidal stability (Fig. 3d). Furthermore, it was found that the hydrodynamic size of GdNPs can be maintained at ultra-diluted concentrations, i.e. 0.1 nM, for 17 days (Fig. 3e). The polydispersity index (PDI) was also recorded over this period. As seen in Fig. 3f, almost all values were lower than 0.3, indicating monodispersity and the stability of **Gd/YbNPs**. The high stability with respect to dissociation in the

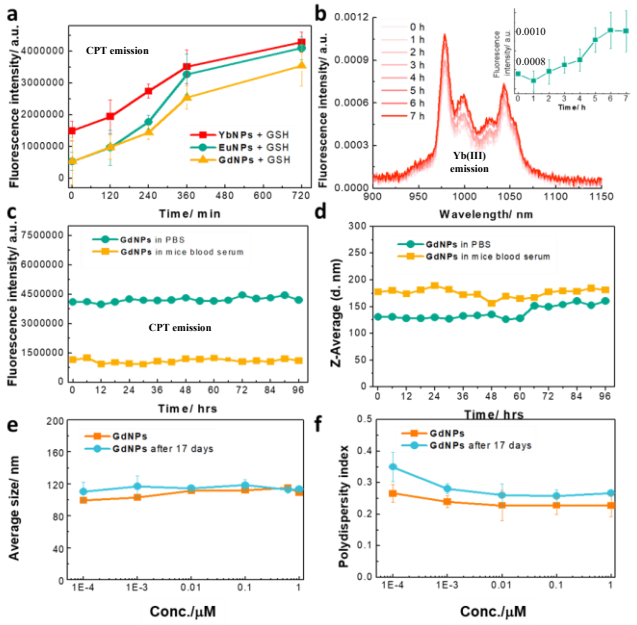

Figure 3. Time-dependent luminescence changes of (a) **LnNPs** at 430 nm (λ_{ex}: 370 nm; **Ln**: **Yb**, **Eu**, **Gd**), and (b) Yb(III) emission of **Gd/YbNPs** (λ_{ex}: 330 nm), in the presence of 2 mM GSH. Inset in (b), time-dependent emission intensity enhancement of **Gd/YbNPs** at 980 nm with 2 mM GSH. [**Gd/YbNPs**] = 10 μM. Measurements were performed in PBS against time. Time dependence of (c) luminescence at 430 nm, and (d) diameter, of **GdNPs** in both PBS (pH = 7.4, 0.1 μM) and mice blood serum (0.2 μM) at 37 ℃ over 4 days. (e) Diameter, and (f) PDI analysis of **GdNPs** at various concentrations in aqueous solution.

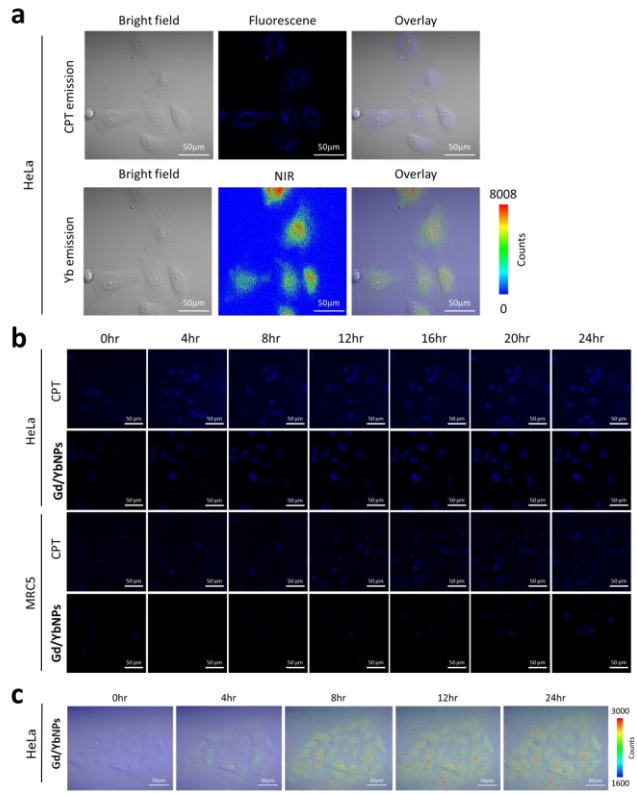

Figure 4. (a) *In vitro* NIR imaging of 5 μM **YbNPs** in HeLa cells (incubation time: 24 hrs; λ_{ex}: 370 nm for CPT emission, detection wavelength range: 400-450 nm; λ_{ex}: 380 nm for Yb(III) emission, detection wavelength range: 900-1700 nm ; scale bar: 50 μm). Time-dependent in vitro emission changes of (b) live imaging signal of the CPT moiety from free CPT only and from **Gd/YbNPs** in HeLa and MRC5 cells (λ_{ex}: 370 nm, detection wavelength range: 400-450 nm; scale bar: 50 μm), and (c) Yb(III) (λ_{ex}: 380 nm) of 5 μM **Gd/YbNPs** by the NIR camera (λ_{ex}: 380 nm, detection wavelength range: 900-1700 nm ; scale bar: 50 μm).

aqueous and *ex vivo* environments, together with the hybrid MR/NIR imaging through combining different Ln ions, makes **Gd/YbNPs** highly attractive as a safe and controllable CPT-delivering platform for cancer therapy.

***In vitro* drug release of Gd/YbNPs.**

Confocal imaging and co-staining experiments were performed to investigate cellular uptake, localization profiles and the *in vitro* CPT release of **Gd/YbNPs**. As seen in Fig. 4a, both the visible CPT emission and NIR Yb(III) emission were observed for **YbNPs** after a 24-hour incubation in HeLa cells, consistent with effective cellular uptake and CPT release. To further evaluate the CPT release, time-dependent confocal imaging studies of **Gd/YbNPs** were performed. As shown in Fig. 4b, **Gd/YbNPs** exhibited a more intense blue CPT emission in HeLa cells than MRC-5 cells at every single time point. Furthermore, the luminescence intensity in HeLa cells gradually enhanced with prolonged incubation times. In contrast, very weak CPT luminescence signals were observed for **Gd/YbNPs** in MRC-5 cells, even after a 24-hour incubation. Time-dependent NIR Yb(III) emission measurements were also performed. As demonstrated in Fig. 4c, GSH treatment also resulted in an obvious increase of the NIR emission in HeLa cells. These results revealed a more efficient release of CPT of **Gd/YbNPs** in cancer cells. Such behavior may be due to the relatively high concentrations of GSH in cancer cell lines, that could induce reductive degradation of the linking disulfide bond. Notably, there was almost no selectivity when it comes to just treating free CPT to HeLa and MRC-5 cells, as it is well known that cellular uptake of CPT is generally good in both normal and cancer cell lines. Taken together these results suggest that the CPT release mechanism in **Gd/YbNPs** has a better selectivity in cancer cells, compared to free CPT.

Encouraged by the *in cellulo* drug release behavior, co-staining experiments were performed to study further the cellular localization of the released CPT of **Gd/YbNPs** (Fig. S11). The merged purple emission in HeLa cells indicated the released CPT was located in the mitochondria, whereas in MRC-5 cells, only red emission from MitoTracker Red was observed and neither blue CPT emission nor merged purple emission were observed, further validating the effective and selective CPT release in cancer cell lines.

***In vivo* MR imaging, bio-distribution and tumor inhibition of Gd/YbNPs.**

After confirming the in vitro NIR emission of **Gd/YbNPs**, we investigated the potential of **Gd/YbNPs** as MRI contrast agents. The contrast-enhanced performance of **Gd/Yb NPs** was first evaluated in water, with the longitudinal relaxivity (r1) measured as 3.7 $mM^{-1}s^{-1}$ (Fig. 5b). The corresponding value of the clinical contrast agent Gd-DOTA was 4.1 $mM^{-1}s^{-1}$, measured under the same conditions (1.4 T, 20°C) (Fig. 5b).[62]. Next, the in vivo MR imaging of mice bearing HeLa xenograft was performed. **Gd/YbNPs** (100 μmol of Gd/kg body weight) were injected via the tail vein; the same amount of Gd-DOTA was injected in a control experiment. The *in vivo* T1-weighted MR images were acquired 24 hours post injection. As seen in Fig. 5a, the HeLa tumor indicated by the red arrow was brightened after injections of **Gd/YbNPs** and by Gd-DOTA. Analysis of the signal enhancement against time showed that **GdNPs** efficiently enhanced the T1 signal in mice bearing HeLa tumor (Fig. S12). To check whether **Gd/YbNPs** can be delivered to the tumor, we further investigated its in vivo biodistribution via ICP-MS. As demonstrated in Fig. 5c, after the intravenous injection, the Gd was detected in most organs, (notably the liver and kidney) and a significant amount was found in the tumor site, but not in the brain, suggesting that **Gd/YbNPs** cannot cross the blood-brain barrier.

Encouraged by the capability of simultaneous NIR imaging and MR imaging, these nanoparticles were further investigated for tumor-inhibition therapy in a HeLa tumor-bearing xenograft model and was compared to CPT. **Gd/YbNPs**, under the same dosage as the in vivo MRI, showed a comparable antitumor effect to CPT and significantly inhibited tumor growth (Fig. 5d). The results demonstrated that the tumor-inhibition efficacy of CPT was maintained by the **Gd/YbNPs** after release *in vivo*.

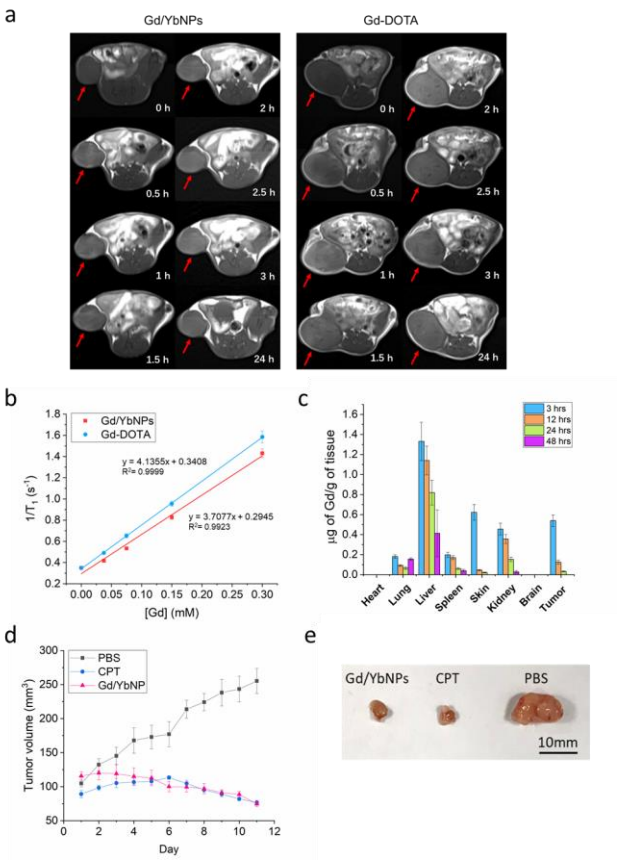

Figure 5. (a) *In vivo* T1-weighted MR images of mice bearing HeLa xenograft from 0–24 hours post injection of **Gd/YbNPs** and Gd-DOTA (control). (b) Plots of 1/T1 vs [Gd] for the determination of r1 of Gd-DOTA and **Gd/YbNPs** hybrid nanoparticles respectively. (c) *In vivo* biodistribution of **Gd/YbNPs** in mice bearing HeLa xenograft via ICP-MS. (d) *In vivo* antitumor activity of **Gd/YbNPs**, 3 mice per group, data are expressed as mean±SEM. (e) Representative photo of tumors treated by **Gd/YbNPs**, CPT and PBS control, scale bar = 10 mm.

Conclusion

In summary, we have demonstrated that the NIR and MR imaging capability of a molecular lanthanide-based nanocomposite can be controlled by incorporating both **cycYb-ss-CPT** and **cycGd-ss-CPT** to form hybrid nanoparticles, with precise control of the Yb and Gd complex ratio in the self-assembly. Conjugated to the complexes by a redox-responsive disulfide bond and encapsulated upon the self-assembly of the amphiphiles, CPT can be released from **cycLn-ss-CPT** *via* the reductive cleavage of the disulfide bond, presumably by the higher concentrations of GSH present in the tumor microenvironment. Such processes were fully and clearly demonstrated by independent DLS, TEM and luminescence analyses. Significant increases of lanthanide emission upon GSH activation were observed in particular, suggesting the *in vitro*/*vivo* CPT drug release

process can be monitored by the high-resolution, Yb(III) NIR imaging.

The formation of nanoparticle structures provided the **cycLn-ss-CPT** amphiphile with high water dispersity and offered CPT protection from degradation. Indeed, the self-assembled **Gd/YbNPs** showed remarkable stability in solution and *ex vivo*. Moreover, **Gd/YbNPs** were found to have superb stability at ultra-diluted concentrations in aqueous solution, i.e. 0.1 nM, for as long as 17 days. The contrast-enhanced performance of **Gd/YbNPs** was confirmed in solution and *in vivo*. The *T*1 contrast-enhanced performance, together with the responsive NIR imaging in cancer cells, offers the enticing prospect of real-time monitoring of the uptake of **Gd/YbNPs** and practical diagnosis of tumors.

It is our objective in this work to provide a strategy to design and construct molecular hybrid nanoparticles from the self-assembly of known ratios of amphiphilic molecular lanthanide macrocycles for imaging capability and drug delivery applications, with the potential to be developed as a functional nanomedicine. Future work exploring behavior with different Ln(III) pairs i.e. Er(III) and Yb(III) to impart up-conversion properties, is ongoing.

ASSOCIATED CONTENT

Supporting Information

The Supporting Information containing the synthesis, experimental methods for critical aggregation concentration measurements, *in vitro* imaging, *in vivo* MRI and tumor inhibition are available free of charge on the ACS Publications website.

AUTHOR INFORMATION

Corresponding Author

* klwong@hkbu.edu.hk
* ga-lai.law@polyu.edu.hk
* lili@sysucc.org.cn
* david.parker@durham.ac.uk

Author Contributions

‡ These authors contribute equally to this work

Notes

The authors declare no competing financial interest.

ACKNOWLEDGMENT

This work was supported by grants from Hong Kong Baptist University (RC-ISRS/17-18/01) and Hong Kong Research Grant Council (HKBU 12309516), Hong Kong Polytechnic University (PolyU 15013/17P), the National Natural Science Foundation of China (NSFC 21728101), the CAS-Croucher Funding Scheme for Joint Laboratories (CAS18204), the Research Foundation of Department of Education of Guangdong Province (2018KTSCX236), the "Hong Kong Scholar" programme, and the China Postdoctoral Science Foundation (2017-015).

REFERENCES

(1) Chen, T.; Pham, H.; Mohamadi, A.; Miller, L. W. Single-chain lanthanide luminescence biosensors for cell-based imaging and screening of protein-protein interactions. IScience, 2020, 23 (9), 101533. https://doi.org/10.1016/j.isci.2020.101533.

(2) Cardoso dos Santos, M.; Colin, I.; Santos, G. R. D.; Susumu, K.; Demarque, M.; Medintz I. L.; Hildebrandt, N. Time-gated FRET nanoprobes for autofluorescence-free long-term in vivo imaging of developing. Adv. Mater., 2020, 32 (39), 2003912. https://doi.org/10.1002/adma.202003912.

(3) Cardodo dos Santos, M.; Runser, A.; Bartenlian, H.; Nonat, A. M.; Charbonnière, L. J.; Klymchenko, A. S.; Hildebrandt, N.; Reisch, A. Lanthanide-complex-loaded polymer nanoparticles for background-free single-particle and live-cell imaging. Chem. Mater., 2019, 31(11), 4034–4041. https://doi.org/10.1021/acs.chemmater.9b00576.

(4) Charpentier, C.; Cifliku, V.; Goetz, J.; Nonat, A.; Cheignon, C.; Cardoso dos Santos, M.; Francés-Soriano, L.; Wong, K.-L.; Charbonnière, L. J.; Hildebrandt, N. Ultrabright terbium nanoparticles for FRET bBiosensing and in situ imaging of epidermal growth factor receptors. Chem. Eur. J., 2020, [doi: 10.1002/chem.202002007].

(5) He, S.; Song, J.; Qu, J.; Cheng, Z. Crucial Breakthrough of Second Near-Infrared Biological Window Fluorophores: Design and Synthesis toward Multimodal Imaging and Theranostics. Chem. Soc. Rev. 2018, 47 (12), 4258–4278. https://doi.org/10.1039/C8CS00234G.

(6) Hong, G.; Antaris, A. L.; Dai, H. Near-Infrared Fluorophores for Biomedical Imaging. Nat. Biomed. Eng. 2017, 1 (1), 0010. https://doi.org/10.1038/s41551-016-0010.

(7) Wales, D. J.; Kitchen, J. A. Surface-Based Molecular Self-Assembly: Langmuir-Blodgett Films of Amphiphilic Ln(III) Complexes. Chem. Cent. J. 2016, 10 (1). https://doi.org/10.1186/s13065-016-0224-6.

(8) Li, Q.; Song, S.; Feng, Z.; Qiu, J.; Sun, M.; Chen, X. Luminescent Vesicles Self-Assembled Directly from an Amphiphilic Europium Complex in an Ionic Liquid. Langmuir 2020, 36 (11),2911–2919. https://doi.org/10.1021/acs.langmuir.0c00007.

(9) Liang, G.; Ronald, J.; Chen, Y.; Ye, D.; Pandit, P.; Ma, M. L.; Rutt, B.; Rao, J. Controlled Self-Assembling of Gadolinium Nanoparticles as Smart Molecular Magnetic Resonance Imaging Contrast Agents. Angew. Chem. Int. Ed Engl. 2011, 50 (28), 6283–6286. https://doi.org/10.1002/anie.201007018.

(10) Yan, R.; Hu, Y.; Liu, F.; Wei, S.; Fang, D.; Shuhendler, A. J.; Liu, H.; Chen, H.-Y.; Ye, D. Activatable

NIR Fluorescence/MRI Bimodal Probes for in Vivo Imaging by Enzyme-Mediated Fluorogenic Reaction and Self-Assembly. J. Am. Chem. Soc. 2019, 141 (26), 10331–10341. https://doi.org/10.1021/jacs.9b03649.

(11) Kaese, T.; Hübner, A.; Bolte, M.; Lerner, H.-W.; Wagner, M. Forming B–B Bonds by the Controlled Reduction of a Tetraaryl-Diborane(6). J. Am. Chem. Soc. 2016, 138 (19), 6224–6233. https://doi.org/10.1021/jacs.6b02303.

(12) Ma, Y.; Mou, Q.; Sun, M.; Yu, C.; Li, J.; Huang, X.; Zhu, X.; Yan, D.; Shen, J. Cancer Theranostic Nanoparticles Self-Assembled from Amphiphilic Small Molecules with Equilibrium Shift-Induced Renal Clearance. Theranostics 2016, 6 (10), 1703–1716. https://doi.org/10.7150/thno.15647.

(13) Yang, Z.; Lin, H.; Huang, J.; Li, A.; Sun, C.; Richmond, J.; Gao, J. A Gadolinium-Complex-Based Theranostic Prodrug for: In Vivo Tumour-Targeted Magnetic Resonance Imaging and Therapy. Chem. Commun. 2019, 55 (31), 4546–4549. https://doi.org/10.1039/C9CC01816F.

(14) Parekh, G.; Pattekari, P.; Joshi, C.; Shutava, T.; DeCoster, M.; Levchenko, T.; Torchilin, V.; Lvov, Y. Layer-by-Layer Nanoencapsulation of Camptothecin with Improved Activity. Int. J. Pharm. 2014, 465 (1–2), 218–227. https://doi.org/10.1016/j.ijpharm.2014.01.041.

(15) Pommier, Y. Topoisomerase I Inhibitors: Camptothecins and Beyond. Nat. Rev. Cancer 2006, 6 (10), 789–802. https://doi.org/10.1038/nrc1977.

(16) Venditto, V. J.; Simanek, E. E. Cancer Therapies Utilizing the Camptothecins: A Review of the in Vivo Literature. Mol. Pharm. 2010, 7 (2), 307–349. https://doi.org/10.1021/mp900243b.

(17) Yanase, K.; Sugimoto, Y.; Tsukahara, S.; Oh-hara, T.; Andoh, T.; Tsuruo, T. Identification and Characterization of a Deletion Mutant of DNA Topoisomerase I MRNA in a Camptothecin-Resistant Subline of Human Colon Carcinoma. Jpn. J. Cancer Res. 2000, 91 (5), 551–559. https://doi.org/10.1111/j.1349-7006.2000.tb00980.x.

(18) Hatefi, A.; Amsden, B. Pharm. Res. 2002, 19 (10), 1389–1399. https://doi.org/10.1023/a:1020427227285.

(19) Wen, Y.; Wang, Y.; Liu, X.; Zhang, W.; Xiong, X.; Han, Z.; Liang, X. Camptothecin-Based Nanodrug Delivery Systems. Cancer Biol. Med. 2017, 14 (4), 363–370. https://doi.org/10.20892/j.issn.2095-3941.2017.0099.

(20) Botella, P.; Rivero-Buceta, E. Safe Approaches for Camptothecin Delivery: Structural Analogues and Nanomedicines. J. Control. Release 2017, 247, 28–54. https://doi.org/10.1016/j.jconrel.2016.12.023.

(21) Chen, K.-J.; Tang, L.; Garcia, M. A.; Wang, H.; Lu, H.; Lin, W.-Y.; Hou, S.; Yin, Q.; Shen, C. K.-F.; Cheng, J.; et al. The Therapeutic Efficacy of Camptothecin-Encapsulated Supramolecular Nanoparticles. Biomaterials 2012, 33 (4), 1162–1169. https://doi.org/10.1016/j.biomaterials.2011.10.044.

(22) Wakabayashi, R.; Ishiyama, R.; Kamiya, N.; Goto, M. A Novel Surface-Coated Nanocarrier for Efficient Encapsulation and Delivery of Camptothecin to Cells. Med. Chem. Comm. 2014, 5 (10), 1515–1519. https://doi.org/10.1039/C4MD00179F.

(23) Schmid, D.; Jarvis, G. E.; Fay, F.; Small, D. M.; Greene, M. K.; Majkut, J.; Spence, S.; McLaughlin, K. M.; McCloskey, K. D.; Johnston, P. G.; et al. Nanoencapsulation of ABT-737 and Camptothecin Enhances Their Clinical Potential through Synergistic Antitumor Effects and Reduction of Systemic Toxicity. Cell Death Dis. 2014, 5 (10), e1454–e1454. https://doi.org/10.1038/cddis.2014.413.

(24) Liu, Y.; Chen, X.; Ding, J.; Yu, L.; Ma, D.; Ding, J. Improved Solubility and Bioactivity of Camptothecin Family Antitumor Drugs with Supramolecular Encapsulation by Water-Soluble Pillar[6]Arene. ACS Omega 2017, 2 (8), 5283–5288. https://doi.org/10.1021/acsomega.7b01032.

(25) Gao, C.; Liang, X.; Mo, S.; Zhang, N.; Sun, D.; Dai, Z. Near-Infrared Cyanine-Loaded Liposome-like Nanocapsules of Camptothecin–Floxuridine Conjugate for Enhanced Chemophotothermal Combination Cancer Therapy. ACS Appl. Mater. Interfaces 2018, 10 (4), 3219–3228. https://doi.org/10.1021/acsami.7b14125.

(26) Wang, H.; Dong, M.; Khan, S.; Su, L.; Li, R.; Song, Y.; Lin, Y.-N.; Kang, N.; Komatsu, C. H.; Elsabahy, M.; et al. Acid-Triggered Polymer Backbone Degradation and Disassembly to Achieve Release of Camptothecin from Functional Polyphosphoramidate Nanoparticles. ACS Macro Lett. 2018, 7 (7), 783–788. https://doi.org/10.1021/acsmacrolett.8b00377.

(27) Chen, M.; Liang, X.; Gao, C.; Zhao, R.; Zhang, N.; Wang, S.; Chen, W.; Zhao, B.; Wang, J.; Dai, Z. Ultrasound Triggered Conversion of Porphyrin/Camptothecin-Fluoroxyuridine Triad Microbubbles into Nanoparticles Overcomes Multidrug Resistance in Colorectal Cancer. ACS Nano 2018, 12 (7), 7312–7326. https://doi.org/10.1021/acsnano.8b03674.

(28) Zolotarskaya, O. Y.; Wagner, A. F.; Beckta, J. M.; Valerie, K.; Wynne, K. J.; Yang, H. Synthesis of Water-Soluble Camptothecin-Polyoxetane Conjugates via Click Chemistry. Mol. Pharm. 2012, 9 (11), 3403–3408. https://doi.org/10.1021/mp3005066.

(29) Cheetham, A. G.; Zhang, P.; Lin, Y.-A.; Lock, L. L.; Cui, H. Supramolecular Nanostructures Formed by Anticancer Drug Assembly. J. Am. Chem. Soc. 2013, 135 (8), 2907–2910. https://doi.org/10.1021/ja3115983.

(30) Wang, J.; Sun, X.; Mao, W.; Sun, W.; Tang, J.; Sui, M.; Shen, Y.; Gu, Z. Tumor Redox Heterogeneity-Responsive Prodrug Nanocapsules for Cancer Chemotherapy. Adv. Mater. 2013, 25 (27), 3670–3676. https://doi.org/10.1002/adma.201300929.

(31) Liu, C.; Yuan, J.; Luo, X.; Chen, M.; Chen, Z.; Zhao, Y.; Li, X. Folate-Decorated and Reduction-Sensitive Micelles Assembled from Amphiphilic Polymer–Camptothecin Conjugates for Intracellular Drug Delivery. Mol. Pharm. 2014, 11 (11), 4258–4269. https://doi.org/10.1021/mp500468d.

(32) Wang, H.; Xie, H.; Wang, J.; Wu, J.; Ma, X.; Li, L.; Wei, X.; Ling, Q.; Song, P.; Zhou, L.; et al. Self-Assembling Prodrugs by Precise Programming of Molecular Structures That Contribute Distinct Stability, Pharmacokinetics, and Antitumor Efficacy. Adv. Funct. Mater. 2015, 25 (31), 4956–4965. https://doi.org/10.1002/adfm.201501953.

(33) Wang, H.; Xu, M.; Xiong, M.; Cheng, J. Reduction-Responsive Dithiomaleimide-Based Nanomedicine with High Drug Loading and FRET-Indicated Drug Release. Chem. Commun. (Camb.) 2015, 51 (23), 4807–4810. https://doi.org/10.1039/C5CC00148J.

(34) Hu, M.; Huang, P.; Wang, Y.; Su, Y.; Zhou, L.; Zhu, X.; Yan, D. Synergistic Combination Chemotherapy of Camptothecin and Floxuridine through Self-Assembly of Amphiphilic Drug–Drug Conjugate. Bioconjug. Chem. 2015, 26 (12), 2497–2506. https://doi.org/10.1021/acs.bioconjchem.5b00513.

(35) He, W.; Hu, X.; Jiang, W.; Liu, R.; Zhang, D.; Zhang, J.; Li, Z.; Luan, Y. Rational Design of a New Self-Codelivery System from Redox-Sensitive Camptothecin-Cytarabine Conjugate Assembly for Effectively Synergistic Anticancer Therapy. Adv. Healthc. Mater. 2017, 6 (24), 1700829. https://doi.org/10.1002/adhm.201700829.

(36) Liu, X.; Shao, W.; Zheng, Y.; Yao, C.; Peng, L.; Zhang, D.; Hu, X.-Y.; Wang, L. GSH-Responsive Supramolecular Nanoparticles Constructed by β-D-Galactose-Modified Pillar[5]Arene and Camptothecin Prodrug for Targeted Anticancer Drug Delivery. Chem. Commun. (Camb.) 2017, 53 (61), 8596–8599. https://doi.org/10.1039/C7CC04932C.

(37) Fang, S.; Hou, Y.; Ling, L.; Wang, D.; Ismail, M.; Du, Y.; Zhang, Y.; Yao, C.; Li, X. Dimeric Camptothecin Derived Phospholipid Assembled Liposomes with High Drug Loading for Cancer Therapy. Colloids Surf. B Biointerfaces 2018, 166, 235–244. https://doi.org/10.1016/j.colsurfb.2018.02.046.

(38) Li, Y.; Kang, T.; Wu, Y.; Chen, Y.; Zhu, J.; Gou, M. Carbonate Esters Turn Camptothecin-Unsaturated Fatty Acid Prodrugs into Nanomedicines for Cancer Therapy. Chem. Commun. (Camb.) 2018, 54 (16), 1996–1999. https://doi.org/10.1039/C8CC00639C.

(39) Yan, C.; Guo, Z.; Shen, Y.; Chen, Y.; Tian, H.; Zhu, W.-H. Molecularly Precise Self-Assembly of Theranostic Nanoprobes within a Single-Molecular Framework for in Vivo Tracking of Tumor-Specific Chemotherapy. Chem. Sci. 2018, 9 (22), 4959–4969. https://doi.org/10.1039/C8SC01069B.

(40) Dong, S.; Sun, Y.; Liu, J.; Li, L.; He, J.; Zhang, M.; Ni, P. Multifunctional Polymeric Prodrug with Simultaneous Conjugating Camptothecin and Doxorubicin for PH/Reduction Dual-Responsive Drug Delivery. ACS Appl. Mater. Interfaces 2019, 11 (9), 8740–8748. https://doi.org/10.1021/acsami.8b16363.

(41) Leroux, J.-C. Editorial: Drug Delivery: Too Much Complexity, Not Enough Reproducibility? Angew. Chem. Int. Ed Engl. 2017, 56 (48), 15170–15171. https://doi.org/10.1002/anie.201709002.

(42) Shi, J.; Kantoff, P. W.; Wooster, R.; Farokhzad, O. C. Cancer Nanomedicine: Progress, Challenges and Opportunities. Nat. Rev. Cancer 2017, 17 (1), 20–37. https://doi.org/10.1038/nrc.2016.108.

(43) Li, F.; Lu, J.; Kong, X.; Hyeon, T.; Ling, D. Dynamic Nanoparticle Assemblies for Biomedical Applications. Adv. Mater. 2017, 29 (14), 1605897. https://doi.org/10.1002/adma.201605897.

(44) Yang, Z.; Song, J.; Tang, W.; Fan, W.; Dai, Y.; Shen, Z.; Lin, L.; Cheng, S.; Liu, Y.; Niu, G.; et al. Stimuli-Responsive Nanotheranostics for Real-Time Monitoring Drug Release by Photoacoustic Imaging. Theranostics 2019, 9 (2), 526–536. https://doi.org/10.7150/thno.30779.

(45) Xu, L.; Yang, Y.; Zhao, M.; Gao, W.; Zhang, H.; Li, S.; He, B.; Pu, Y. A Reactive Oxygen Species–Responsive Prodrug Micelle with Efficient Cellular Uptake and Excellent Bioavailability. J. Mater. Chem. B Mater. Biol. Med. 2018, 6 (7), 1076–1084. https://doi.org/10.1039/C7TB02479G.

(46) Pei, P.; Sun, C.; Tao, W.; Li, J.; Yang, X.; Wang, J. ROS-Sensitive Thioketal-Linked Polyphosphoester-Doxorubicin Conjugate for Precise Phototriggered Locoregional Chemotherapy. Biomaterials 2019, 188, 74–82.
https://doi.org/10.1016/j.biomaterials.2018.10.010.

(47) Wang, Y.; Wei, G.; Zhang, X.; Xu, F.; Xiong, X.; Zhou, S. A Step-by-Step Multiple Stimuli-Responsive Nanoplatform for Enhancing Combined Chemo-Photodynamic Therapy. Adv. Mater. 2017, 29 (12), 1605357. https://doi.org/10.1002/adma.201605357.

(48) Shi, X.; Hou, M.; Bai, S.; Ma, X.; Gao, Y.-E.; Xiao, B.; Xue, P.; Kang, Y.; Xu, Z.; Li, C. M. Acid-Activatable Theranostic Unimolecular Micelles Composed of Amphiphilic Star-like Polymeric Prodrug with High Drug Loading for Enhanced Cancer Therapy. Mol. Pharm. 2017, 14 (11), 4032–4041. https://doi.org/10.1021/acs.molpharmaceut.7b00704.

(49) Chen, H.; Tham, H. P.; Ang, C. Y.; Qu, Q.; Zhao, L.; Xing, P.; Bai, L.; Tan, S. Y.; Zhao, Y. Responsive Prodrug Self-Assembled Vesicles for Targeted Chemotherapy in Combination with Intracellular Imaging. ACS Appl. Mater. Interfaces 2016, 8 (37), 24319–24324. https://doi.org/10.1021/acsami.6b08044.

(50) Huang, P.; Wang, D.; Su, Y.; Huang, W.; Zhou, Y.; Cui, D.; Zhu, X.; Yan, D. Combination of Small Molecule Prodrug and Nanodrug Delivery: Amphiphilic Drug–Drug Conjugate for Cancer Therapy. J. Am. Chem. Soc.

2014, 136 (33), 11748–11756. https://doi.org/10.1021/ja505212y.

(51) MacKay, J. A.; Chen, M.; McDaniel, J. R.; Liu, W.; Simnick, A. J.; Chilkoti, A. Self-Assembling Chimeric Polypeptide-Doxorubicin Conjugate Nanoparticles That Abolish Tumours after a Single Injection. Nat. Mater. 2009, 8 (12), 993–999. https://doi.org/10.1038/nmat2569.

(52) Wu, X.; Sun, X.; Guo, Z.; Tang, J.; Shen, Y.; James, T. D.; Tian, H.; Zhu, W. In vivo and in situ Tracking Cancer Chemotherapy by Highly Photostable NIR Fluorescent Theranostic Prodrug. J. Am. Chem. Soc. 2014, 136 (9), 3579–3588. https://doi.org/10.1021/ja412380j.

(53) Guo, X.; Shi, C.; Yang, G.; Wang, J.; Cai, Z.; Zhou, S. Dual-Responsive Polymer Micelles for Target-Cell-Specific Anticancer Drug Delivery. Chem. Mater. 2014, 26 (15), 4405–4418. https://doi.org/10.1021/cm5012718.

(54) Zhang, Q.; He, J.; Zhang, M.; Ni, P. A Polyphosphoester-Conjugated Camptothecin Prodrug with Disulfide Linkage for Potent Reduction-Triggered Drug Delivery. J. Mater. Chem. B Mater. Biol. Med. 2015, 3 (24), 4922–4932. https://doi.org/10.1039/C5TB00623F.

(55) Han, H.; Wang, H.; Chen, Y.; Li, Z.; Wang, Y.; Jin, Q.; Ji, J. Theranostic Reduction-Sensitive Gemcitabine Prodrug Micelles for near-Infrared Imaging and Pancreatic Cancer Therapy. Nanoscale 2016, 8 (1), 283–291. https://doi.org/10.1039/C5NR06734K.

(56) Su, H.; Zhang, P.; Cheetham, A. G.; Koo, J. M.; Lin, R.; Masood, A.; Schiapparelli, P.; Quiñones-Hinojosa, A.; Cui, H. Supramolecular Crafting of Self-Assembling Camptothecin Prodrugs with Enhanced Efficacy against Primary Cancer Cells. Theranostics 2016, 6 (7), 1065–1074. https://doi.org/10.7150/thno.15420.

(57) Luo, C.; Sun, J.; Sun, B.; Liu, D.; Miao, L.; Goodwin, T. J.; Huang, L.; He, Z. Facile Fabrication of Tumor Redox-Sensitive Nanoassemblies of Small-Molecule Oleate Prodrug as Potent Chemotherapeutic Nanomedicine. Small 2016, 12 (46), 6353–6362. https://doi.org/10.1002/smll.201601597.

(58) Xing, L.; Zhang, J.-L.; Zhou, T.-J.; He, Y.-J.; Cui, P.-F.; Gong, J.-H.; Sun, M.; Lu, J.-J.; Huang, Z.; Jin, L.; et al. A Novel Design of a Polynuclear Co-Delivery System for Safe and Efficient Cancer Therapy. Chem. Commun. (Camb.) 2018, 54 (63), 8737 – 8740. https://doi.org/10.1039/C8CC03720E.

(59) Chen, D.; Zhang, G.; Li, R.; Guan, M.; Wang, X.; Zou, T.; Zhang, Y.; Wang, C.; Shu, C.; Hong, H.; et al. Biodegradable, Hydrogen Peroxide, and Glutathione Dual Responsive Nanoparticles for Potential Programmable Paclitaxel Release. J. Am. Chem. Soc. 2018, 140 (24), 7373–7376. https://doi.org/10.1021/jacs.7b12025.

(60) Lu, Y.; Yue, Z.; Xie, J.; Wang, W.; Zhu, H.; Zhang, E.; Cao, Z. Micelles with Ultralow Critical Micelle Concentration as Carriers for Drug Delivery. Nat. Biomed. Eng. 2018, 2 (5), 318–325. https://doi.org/10.1038/s41551-018-0234-x.

(61) Owen, S. C.; Chan, D. P. Y.; Shoichet, M. S. Polymeric Micelle Stability. Nano Today 2012, 7 (1), 53–65. https://doi.org/10.1016/j.nantod.2012.01.002.

(62) Debroye, E.; Eliseeva, S. V.; Laurent, S.; Elst, L. V.; Muller, R. N.; Parac-Vogt, T. N. Micellar Self-Assemblies of Gadolinium(III)/Europium(III) Amphiphilic Complexes as Model Contrast Agents for Bimodal Imaging. Dalton Trans. 2014, 43 (9), 3589–3600. https://doi.org/10.1039/C3DT52842A.

(63) Clough, T. J.; Jiang, L.; Wong, K.-L.; Long, N. J. Ligand Design Strategies to Increase Stability of Gadolinium-Based Magnetic Resonance Imaging Contrast Agents. Nat. Commun. 2019, 10 (1), 1420. https://doi.org/10.1038/s41467-019-09342-3.

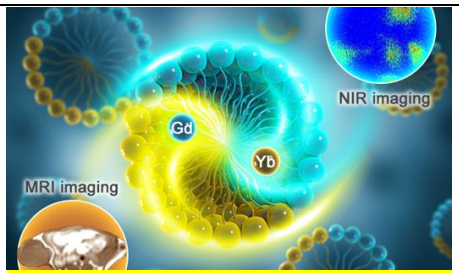

Table of Contents